Int J Adv Manuf Technol (2015) 77:341–355
DOI 10.1007/s00170-014-6453-8

ORIGINAL ARTICLE

Generalized cutting force model in multi-axis milling using a new engagement boundary determination approach

Tunç Lütfi Taner · Özkirimli Ömer · Budak Erhan

Received: 25 April 2014 / Accepted: 30 September 2014 / Published online: 16 October 2014

Abstract Simulation of cutting processes provides valuable insight into machining applications which have complex mechanics. In this paper, a generalized cutting force model is proposed for multi-axis milling operations. In the proposed model, the cutting tool envelope is defined either as revolution of a multi-segmented curve or using seven-parameter milling tool definition. The engagement between the cutting tool envelope and workpiece is calculated using a new, robust, and fast approach based on projective geometry. Exact chip thickness expression is used to simulate cutting kinematics for all types of edge geometries, such as serrated, variable pitch, and variable helix cutting flutes. The performance of the method proposed for determination of engagement boundaries is discussed through calculation time studies under several conditions. The predictions are verified and discussed through cutting experiments, conducted at multi-axis machining conditions using various cutting tool geometries.

Keywords Process modeling · Multi-axis milling · Cutting forces

1 Introduction

Multi-axis milling is widely used in machining of parts involving complex features such as the ones designed in aerospace, automotive, die, and mold industries. Selection of cutting parameters is very crucial to achieve increased productivity and part quality in such industries, where high cost of raw material, equipment, and tooling involved. Thus, a detailed understanding of the process is essential. However, this is not a straightforward task as several aspects such as geometry, kinematics, and mechanics of multi-axis milling are complicated. Process models can be used to analyze effects of tool geometry and cutting conditions on the process for selection of the correct tooling and parameter set.

Extensive amount of work has been done on the mechanics of milling for different tool types. The mechanics of flat end milling was first examined by Martelotti [1]. Later, Koenigsberger and Sabberwal [2] developed equations for milling forces based on mechanistic modeling. Kline et al. [3] extended this approach and calculated cutting forces by modeling chip load and cutting geometry for milling to predict associated machine component deflections and form errors. Later, Altintas and Spence [4] developed a semi-analytical force model which can be integrated into CAD systems. Budak et al. [5] proposed a cutting coefficient prediction method for helical end milling based on orthogonal-to-oblique transformation approach introduced earlier by Armarego et al. [6]. Lee and Altintas [7] modeled the mechanics and dynamics of helical ball end mills employing this model. Engin and Altintas [8, 9] proposed the first model for mechanics and dynamics of three-axis milling with generalized cutters, where helical cutting edges are modeled to be wrapped around the tool envelope. Merdol and Altintas [10] developed a cutting force model for serrated flat and taper end mills. They used the force model for time domain simulation of stability of serrated cutters. Nonetheless, all of the above models are limited to three-axis operations for cutting tools with regular cutting edges. Later, Kaymakci et al. [11] developed a unified mechanistic model for turning, boring, drilling, and milling operations where transformation to the cutting edge is applied with respect to the process in focus. This study can be considered as one of the first attempts to develop a generalized cutting force model for different types of cutting tools.

Determination of the engagement boundary between the cutter and workpiece is essential for simulation of mechanics and dynamics of five-axis milling operations. The process geometry becomes complicated as the number of simultaneous axes increases in milling. In two-and-a-half-axis flat end milling and even in three-axis ball end milling, the

T. L. Taner · Ö. Ömer · B. Erhan (✉)
Manufacturing Research Lab, Sabanci University, Istanbul, Turkey
e-mail: ebudak@sabanciuniv.edu

engagement boundary can be calculated analytically [4]. Lazoglu and Liang [12] proposed one of the first models for three-axis ball end milling of sculptured surfaces using analytical calculation of the engagement boundaries, which is verified by airfoil machining experiments. However, in five-axis milling with generalized cutter geometry, it is almost impossible to determine the engagement boundary using an analytical method. A semi-analytical cutting force model for five-axis ball end milling is developed by Ozturk and Budak [13], which is an improvement of the geometrical model proposed by Lee and Altintas [14]. A semi-analytical model for taper ball end mills used in the manufacturing of integrally bladed disks for aerospace industry is proposed by Ferry and Altintas [15]. Lopez de Lacalle et al. [16] modeled cutting forces and tool deflection in ball end milling. In almost all of the studies on modeling of cutting forces in multi-axis milling, it is reported that determination of engagement boundaries is one of the key points for the generality of the proposed model. Moreover, it is also reported that determination of engagement boundaries takes the most part of the calculation time. Considering this essential essentiality, in this paper, a method, based on projective geometry, is proposed for determination of engagement boundaries in five-axis milling with general cutter definition. It can be concluded that the previous studies propose custom models for specific cases, i.e., ball end mills [12, 14], taper ball end mills [15, 17], serrated flat end mills [18], general end mills [8], and inserted milling tools [9, 19, 20].

As summarized in this section, there have been several studies on geometry and mechanics of multi-axis milling with different tool geometries and milling applications. In this paper, a general process model for simulation of cutting forces in multi-axis milling is presented. In the model, generalized cutter definition is used with generalized cutting edge definition such as serrated, variable helix, and variable pitch tools. This is an important effort to achieve a unified model which can be used for simulation of cutting forces in multi-axis milling with generalized cutter geometry which has general cutting flute geometry. Moreover, by use of such a generalized model, effects of cutting parameters and tool geometry can be understood easily by comparing different conditions through simulations. The paper is organized as follows; the generalized milling tool geometry is presented in Sect. 2, which is followed by the engagement model in Sect. 3. The force model and experimental validation results are presented in Sects. 4 and 5, respectively.

2 Milling tool geometry

Modeling of multi-axis milling requires the cutting tool to be geometrically defined, where the cutter can be considered as a revolution of an arbitrary section curve around the tool axis, resulting in a volumetric tool envelope. The tool envelope is then divided into axial and radial segments to be represented as an organized point cloud. The section curve representing the tool radial boundary can be defined by either connected points or standard seven-parameter milling tool definition as shown in Fig. 1.

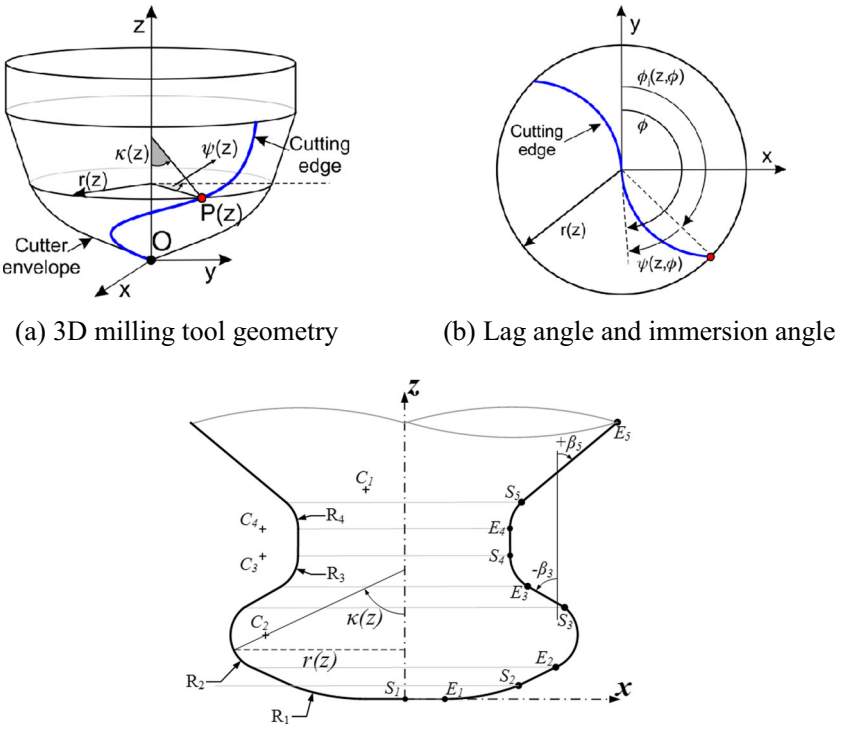

(a) 3D milling tool geometry

(b) Lag angle and immersion angle

(c) Sample multi-segmented tool profile.

Fig. 1 Generalized milling tool and corresponding geometrical parameters. **a** 3D milling tool geometry. **b** Lag angle and immersion angle. **c** Sample multi-segmented tool profile

A point $P(z)$ on a helical cutting flute is defined in cylindrical coordinates in terms of radial distance $r(z)$, the radial lag angle $\psi(z)$, and the axial immersion angle $\kappa(z)$, i.e., the angle between the tool axis and the cutting edge normal, as shown in Fig. 1a. There is rotational lag angle, $\psi(z)$, between consecutive points on the helical cutting edge due to helix angle as shown in Fig. 1b. The immersion angle of any point on the helical cutting edge is written in terms of the lag angle and the cutter rotation angle, ϕ. For general cutting tools with variable helix and variable tooth pitch separation, the generalized local immersion angle $\phi_j(z)$ for the j^{th} cutting edge is written as follows:

$$\phi_j(z) = \phi + \phi_{p,j} - \psi_j(z) \tag{1}$$

where $\phi_{p,j}$ and ψ_j represent the pitch angle of the j^{th} cutting edge with respect to the previous $(j\text{-}1)^{th}$ one and the axial lag angle of the j^{th} cutting edge at level z, respectively. The parameters used to express the immersion angle depend on the tool profile which is explained for the general cutter geometry in the next section.

2.1 Definition of multi-segmented tools

In general, solid milling tools can be considered as union of basic geometric 3D units which are tori and cones. Standard milling tools can be represented parametrically [8] as they are union of three or less segments. However, it becomes hard and inefficient to represent custom tools having intricate multi-segmented, i.e., union of more than three basic geometric units, geometries as illustrated in Fig. 1c. It is rather more convenient to obtain the section curve to be revolved, from one of the standard CAD data formats. So that, the cross section of the cutter envelope is modeled as combination of lines and arcs corresponding to each segment. Initial Graphics Exchange Specification (IGES) data format is adequate for obtaining the boundary information of the individual segments. An exemplary multi-segmented tool geometry involving four arcs and five lines with corresponding geometrical parameters is given in Fig. 1c. Any segment j can be defined by either a line starting at point S_j and ending at point E_j, or an arc centered at point C_j.

The radial distance $r(z)$ and the axial immersion angle $\kappa(z)$ for a linear segment are given as follows:

$$\left.\begin{aligned} r(z) &= \frac{z - S_{j,z}}{\tan\beta_j} + S_{j,x} \\ \kappa(z) &= \beta_j \end{aligned}\right\} \tag{2}$$

where β_j is the inclination angle of the line segment j.

The conic part of a tapered milling tool is represented by a line segment considering the differential equation formulation given for a helical flute wrapping a cone by Ramaraj [21], where the lag angle definition is given as follows:

$$\psi_L = \frac{\ln(r(z))\tan i_0}{\sin\beta_j} \tag{3}$$

A circular cross section is used to represent a torus unit element in the cutter envelope, where the radial distance $r(z)$ and the axial immersion angle $\kappa(z)$ are given as follows:

$$\left.\begin{aligned} r(z) &= \sqrt{R^2 - (R_{z,s} - z)^2} \\ \kappa(z) &= \sin^{-1}\left(\frac{r(z) - R_{r,s}}{R}\right) \end{aligned}\right\} \tag{4}$$

The lag angle for the arc segment is expressed as follows:

$$\psi_A = \frac{(R_j - C_{j,z} + z)\tan i_0}{R_j} \tag{5}$$

Final lag angle at elevation z is calculated between consecutive segments for continuity;

$$\psi(z) = \psi_{L/A} + \psi_{pre} - \psi_{cur} \tag{6}$$

where ψ_{pre} is the final lag angle of the previous segment at the starting point of the current one and ψ_{cur} is the lag angle of the current segment at its starting point. Sample tool envelopes extracted from IGES data and constructed 3D cutter body with helical cutting flutes are shown in Fig. 2.

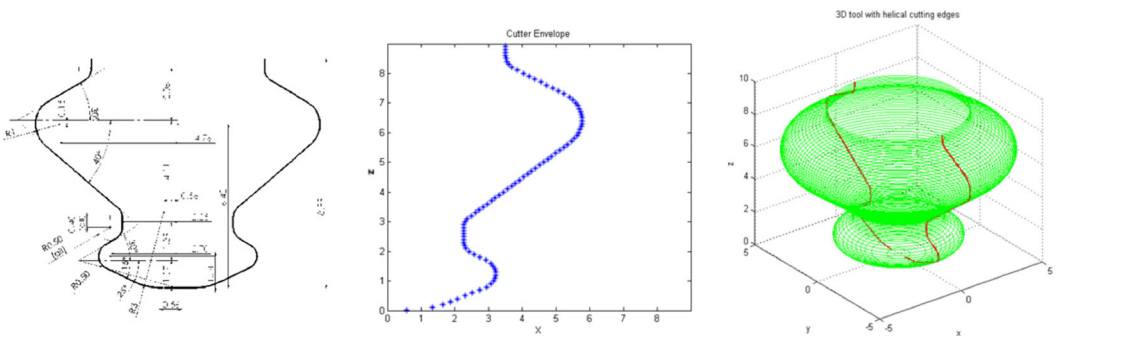

(a) CAD Model (b) Cutter Envelope (c) Cutter & Cutting Flutes, 3D view

Fig. 2 Example of multi-segmented cutter representation with cutting flutes. **a** CAD model. **b** Cutter envelope. **c** Cutter and cutting flutes, 3D view

2.2 Modeling of nonuniform cutting flute geometry

In machining, it is well known that cutting tools with irregular cutting edges such as variable pitch, variable helix, or serrated tools are used for increased cutting performance [22]. The nonuniform cutting edge geometry makes the chip thickness variable along the tool axis, as well. As a result, the cutting forces are leveled over a revolution, and the overstability increases. In this section, the irregular cutting edge geometry to represent such cases is given.

2.2.1 Variable pitch and variable helix tools

In general, the helix angle and/or the pitch angle may change between consecutive flutes as shown in Fig. 3. The immersion angle is given in Eq. (1), and hence the instantaneous chip thickness at any axial level along the cutter axis depends on the helix angle and the pitch angle of the corresponding flute. The mechanics and dynamics of milling process are affected by the instantaneous chip thickness and the time delay between successive cutting teeth passes. Therefore, it is of great importance to account the variation of helix and pitch angles for generality of the proposed model. For such a purpose, Eq. (1) is examined in two parts. First, the variation of the pitch angle is denoted by $\phi_{p,j}$ representing the angular position of the j^{th} cutting edge with respect to previous $j\text{-}1^{th}$ edge. Secondly, the lag angle for level z of the j^{th} cutting edge is represented by $\psi_j(z)$ depending on the helix angle of the j^{th} cutting edge, $i_{o,j}$.

The time delay between successive cutting passes at elevation z is written in terms of the separation angle, $\delta\phi_j(z)$, which is the difference in the angular position of consecutive flutes, and it is calculated as the difference of immersion angle (refer to Eq.(1)) of j^{th} and $j+1^{th}$ flute;

$$\delta\phi_j(z) = \phi_{j+1}(z) - \phi_j(z) \tag{7}$$

In this study, two common variation patterns are considered for pitch angle distribution, which are linear and alternating. For both cases, a pitch angle variation measure, ΔP, is introduced, and the initial pitch angle is found as follows:

$$\left.\begin{aligned} &P_0, P_0+\Delta P, P_0+2\Delta P, \ldots, P_0+(N_t-1)\Delta P \\ &P_0 = \frac{2\pi}{N_t} - \frac{(N_t-1)\Delta P}{2} \end{aligned}\right\} \textit{Linear} \tag{8}$$

$$\left.\begin{aligned} &P_0, P_0+\Delta P, P_0, \ldots, P_0+\begin{cases} \Delta P & N_t \text{ even} \\ 0 & N_t \text{ odd} \end{cases} \\ &P_0 = \frac{2\pi}{N_t} - \frac{\Delta P}{N_t}\sum_{k=1}^{N_t}\left((-1)^k+1\right) \end{aligned}\right\} \text{Alternating} \tag{9}$$

3 Determination of cutter workpiece engagement boundary

The engagement between cutting tool and workpiece mainly depends on the cutting tool geometry and process parameters such as step over, cutting depth, lead, and tilt angles as these parameters define the position of the cutting tool with respect to the workpiece as illustrated in Fig. 4. It is seen that CWEB drastically changes with any of the named parameters. Thus, it is hard and almost impossible to classify such a behavior case by case especially for a generalized cutting tool geometry.

Geometry of the cubic workpiece is modeled considering two basic cases as shown in Fig. 4a, b, where in the first case, the workpiece uncut surface is planar and in the second case, the uncut surface is generated by a previous cutting step. In the first cut case, the workpiece boundary in cross feed direction (C) is a line, whereas in the following cut case, the workpiece boundary in cross feed direction (C) is duplication of the cutter boundary, which

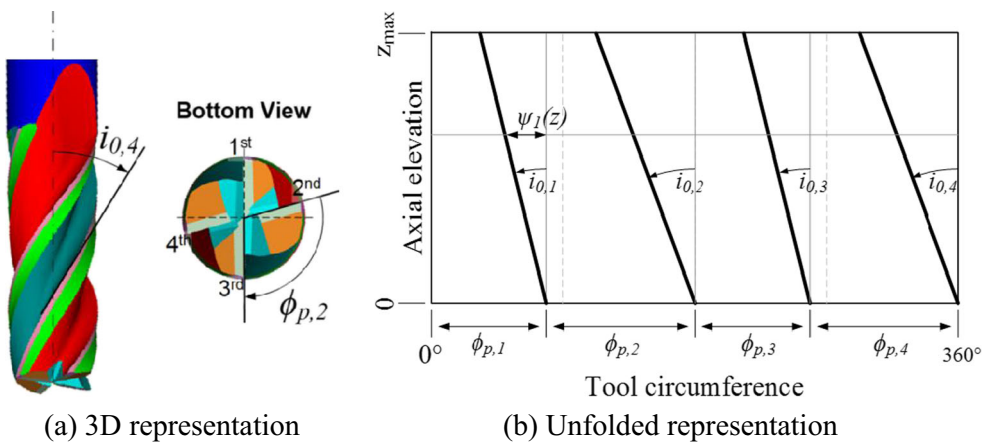

(a) 3D representation (b) Unfolded representation

Fig. 3 Cutting flute geometry and corresponding parameters. **a** 3D representation. **b** Unfolded representation

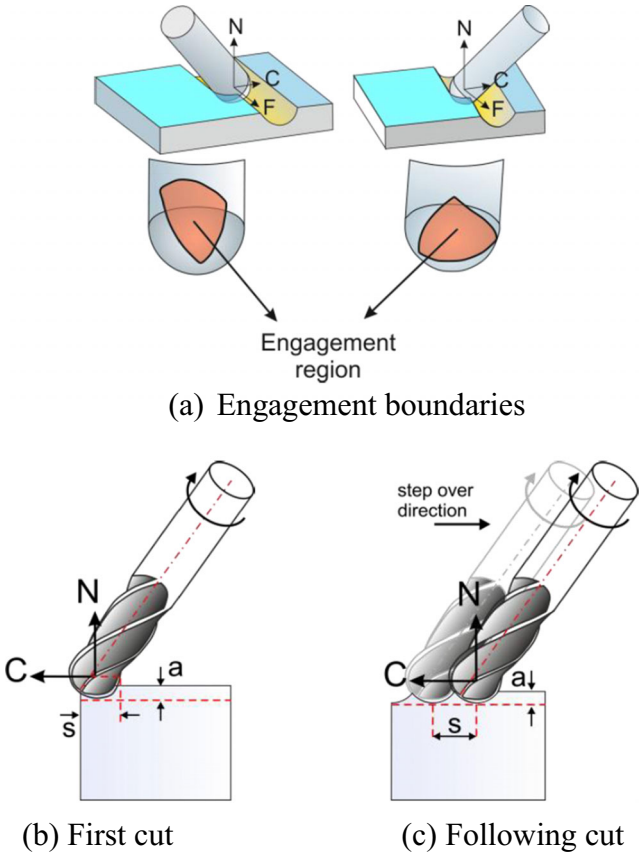

Fig. 4 Engagement boundaries at different cases in five-axis milling. **a** Engagement boundaries. **b** First cut. **c** Following cut

is left from the previous cutting pass. In this section, the approach proposed for determination of CWEB is presented.

3.1 Projective geometry method

The proposed CWEB algorithm is mainly based on the projective geometry, where the boundaries of the cutting tool and cubic workpiece are projected onto XZ plane and YZ plane as shown in Fig. 5. Here, it is noteworthy to state that X, Y, and Z directions correspond to the feed F, cross feed C, and workpiece surface normal N directions, respectively. The condition of any point on the tool envelope to be engaged with the workpiece is satisfied when the corresponding point is in the bounds of the workpiece both in XZ and YZ planes. For such a purpose, point in polygon (PIP) algorithm [23] makes it easy to check all points in once whether they are in the workpiece boundaries when projected onto the corresponding plane. So, the first check is performed in XZ projection plane as illustrated in Fig. 5a. Then, only the points which are in the boundaries of –XZ projection of the workpiece are tested for –YZ projection as shown in Fig. 5b. Finally, the cutter engagement boundary is mapped in axial and radial coordinates of the cutting tool as shown in Fig. 5c. The cutting tool, cubic workpiece, and CWEB are plotted in 3D in Fig. 5d.

3.2 Performance evaluation

In the literature, it is well reported that the performance of discrete models is nonlinearly affected by the discretization and process parameters. This is mainly due to the fact that the engagement boundary algorithms depend on the number of discretized elements as they search each and every discrete element for engagement. As a result of this, the computation time drastically increases as the precision increases. In this section, the performance of the proposed CWEB algorithm is analyzed, and the results are evaluated based on the conditions given in Table 1.

The CWEB algorithm is executed with different cutting parameters and precision settings on MATLAB© installed on a computer with Intel© I7 CPU, 8 GB of RAM, where the computation time for different cases is compared in Fig. 6. It is seen that in most of the cases, the computation time is shorter than 0.05 s. The computation time increases up to 0.15 s in some cases, for increased cutting depth or very small discretization parameters. Though, the behavior of computation time shows a linear variation with cutting parameters and precision settings.

In Fig. 6a, the effect of cutting depth on computation time is plotted with different radial discretization settings ($d\phi$). It is seen that the computation time linearly increases with cutting depth and it is mostly below 0.05 s except for the case where $d\phi=1°$. In Fig. 6b, the change of computation time with step over, with different radial discretization settings, is plotted. It is seen that the computation time is not almost affected by step over value, where it is mostly less than 0.05 s, again except for the case where $d\phi=1°$. The change in computation time with axial and radial discretization of the cutting tool is also plotted in Fig. 6c, d, respectively. It is observed that the computation time changes linearly with discretization settings, where again in most cases, it is less than 0.05 s.

The performance evaluation results show that the proposed CWEB algorithm performs with linear time complexity without loss of any generality contrary to most of the discretization methods. The proposed CWEB algorithm is used in integration with the mechanistic cutting force model, which is detailed in the next section.

4 Modeling of cutting forces

Modeling of milling processes requires the chip thickness to be defined and related to the cutting forces. In

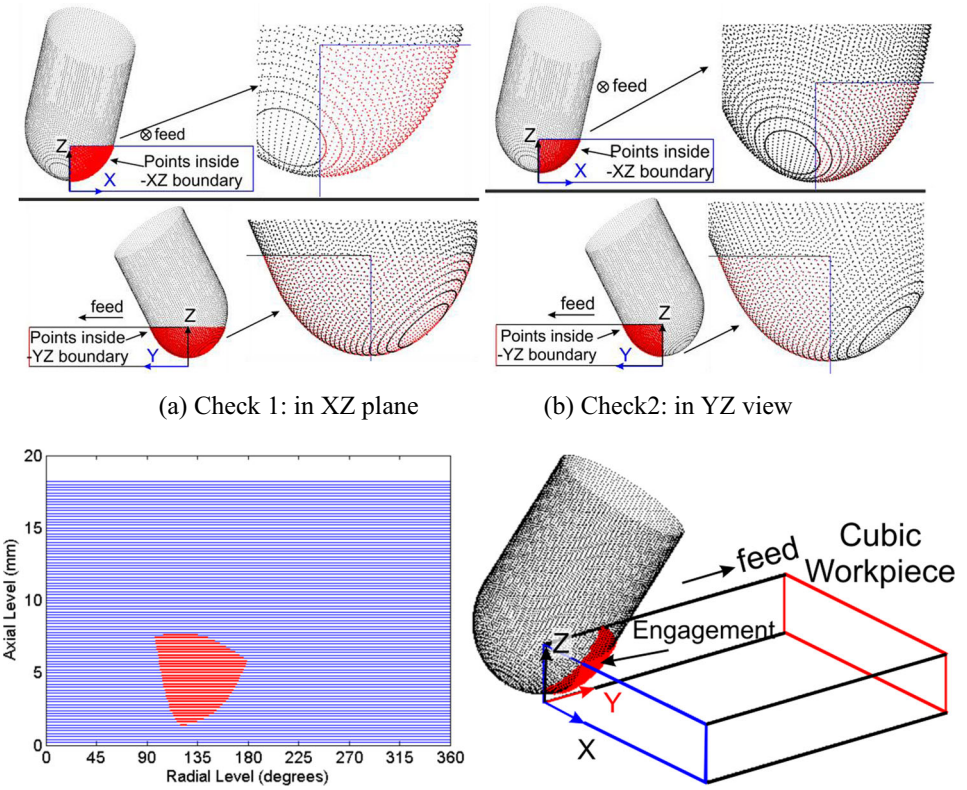

Fig. 5 Projection of tool and workpiece boundaries. **a** Check 1 in XZ plane. **b** Check 2 in YZ view. **c** Engagement boundaries in axial and radial map. **d** 3D view of engagement region

(a) Check 1: in XZ plane (b) Check2: in YZ view

(c) Engagement boundaries in axial and radial map (d) 3D view of engagement region

this study, the cutting forces are modeled using oblique-to-orthogonal cutting transformation where the orthogonal cutting force parameters are derived through thermomechanical process model [24, 25]. Then, the differential cutting forces acting at a point P on the j^{th} cutting edge are calculated by knowing the local chip thickness as illustrated in Fig. 7. Point P is defined in cylindrical coordinates by its elevation from the tool tip along the tool axis, z, and the radial immersion $\phi_j(\phi,z)$. In this section, the cutting force model is summarized together with the chip thickness definition used in the model.

Table 1 Cutting conditions for performance evaluation

Tool type	Ball end mill
Tool diameter (mm)	12
No. of Flutes	4
Helix angle (deg)	30
Cutting depth (mm)	12
Step over (mm)	6
Cutting mode	Down
Lead/tilt angle (deg)	30/15
dZ (mm)	0.2
dPhi (deg)	3

4.1 Mechanistic force model

Differential cutting forces in the radial, axial, and tangential directions on an axial disc of the j^{th} tooth at elevation z and at rotation angle ϕ_j are calculated according to the mechanistic model proposed by Lee and Altintas [7]. Differential cutting forces are the summation of the cutting forces due to shearing mechanism and ploughing (edge) forces due to the friction at rake face and flank face of the tool.

$$\begin{bmatrix} dF_{r_j}(z) \\ dF_{t_j}(z) \\ dF_{a_j}(z) \end{bmatrix} = \begin{bmatrix} K_{rc}h_j(\phi_j,z)\mathrm{d}b + K_{re}\mathrm{d}S_j \\ K_{tc}h_j(\phi_j,z)\mathrm{d}b + K_{te}\mathrm{d}S_j \\ K_{ac}h_j(\phi_j,z)\mathrm{d}b + K_{ae}\mathrm{d}S_j \end{bmatrix} \cdot \delta(z) \quad (10)$$

where,

$$\delta(z) = \begin{cases} 1 \; if \; P(z,\phi_j) \in CEB(\phi,z) \\ 0 \; if \; P(z,\phi_j) \notin CEB(\phi,z) \end{cases}$$

K_{rc}, K_{tc}, and K_{ac}, and K_{re}, K_{te}, and K_{ae} are the cutting and edge force coefficients, respectively. An accurate semi-analytical methodology is used to predict these coefficients employing thermomechanical cutting process model [24, 25] and orthogonal-to-oblique transformation [5]. Thermomechanical dual zone model is used to predict orthogonal cutting force coefficients (i.e., shear angle ϕ_s, shear stress

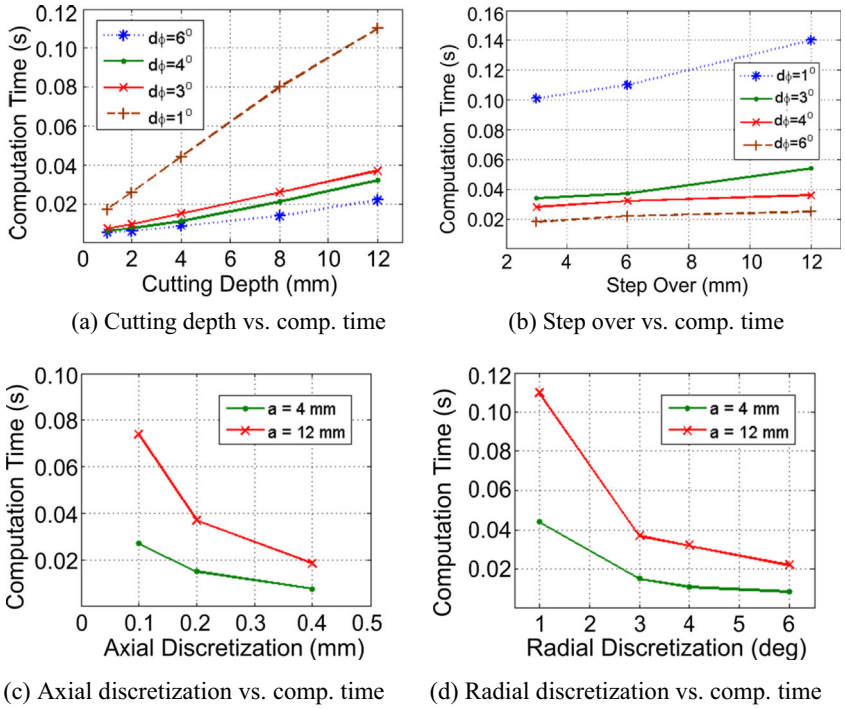

(a) Cutting depth vs. comp. time (b) Step over vs. comp. time

(c) Axial discretization vs. comp. time (d) Radial discretization vs. comp. time

Fig. 6 Performance analysis of the algorithm. **a** Cutting depth vs. comp. time. **b** Step over vs. comp. time. **c** Axial discretization vs. comp. time. **d** Radial discretization vs. comp. time

τ_1, and apparent friction coefficient μ_c Eq. (11)) using the Johnson-Cook material model considering the stick-slide regions on the rake face.

$$\mu_c = \frac{\tau_1}{P_0}\left[1+\zeta\left(1-\left(\frac{\tau_1}{P_0\mu_s}\right)^{\frac{1}{\zeta}}\right)\right] \tag{11}$$

Sliding friction coefficient as a function of cutting velocity V_{cut} is obtained from orthogonal tube cutting tests with varying feeds and cutting speeds to obtain edge force coefficients K_{re}, K_{te}, and K_{ae}. The sliding friction coefficient, μ_s, derived from apparent friction coefficient measured during the tests

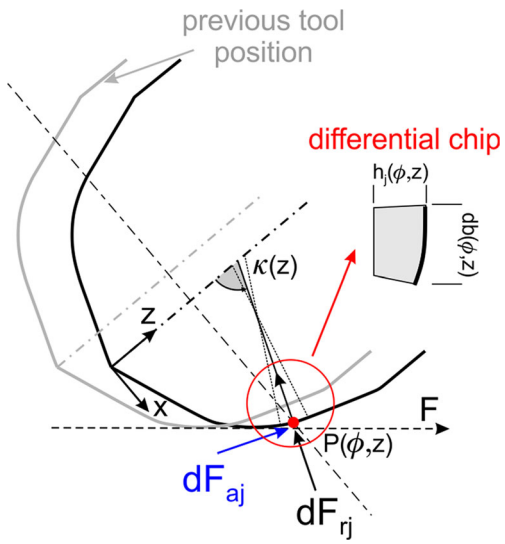

Fig. 7 Differential cutting forces and chip thickness in multi-axis milling

with the iterative solution procedure presented in [24]. Thus, the variation of the local rake angle on the helix flute can be modeled and considered in the force model. After obtaining the orthogonal cutting force coefficients by the thermomechanical model, they are transformed to oblique cutting using the model presented in [5] where normal friction angle β_n, normal rake angle α_n, and chip flow angle η_c are considered;

$$\begin{bmatrix} dF_{tc} \\ dF_{rc} \\ dF_{ac} \end{bmatrix} = db.h_j. \begin{bmatrix} K_{tc} \\ K_{rc} \\ K_{ac} \end{bmatrix}$$

$$= db.h_j. \begin{bmatrix} \tau_1 \dfrac{\cos(\beta_n-\alpha_n)+\tan\alpha_n\tan\eta_c\sin\beta_n}{C} \\ \tau_1 \dfrac{\sin(\beta_n-\alpha_n)}{C\cos\alpha_n} \\ \tau_1 \dfrac{\cos(\beta_n-\alpha_n)\tan\alpha_n-\tan\eta_c\sin\beta_n}{C} \end{bmatrix} \tag{12}$$

where

$$C = \sin\phi_n\sqrt{\cos^2(\phi_n+\beta_n-\alpha_n)+\tan^2\eta_c\sin\beta_n}$$
$$\beta_n = \mu_c\cos\eta_c \tag{13}$$

Utilizing these predictive models an average discrepancy of 7 % is obtained between the simulations and measurements [25]; however, thanks to robustness of these models with a

simple orthogonal tube test, a force model can be constituted to predict the cutting behavior for all cutting geometries.

Chip thickness $h_j(\phi_j,z)$ and chip width db_j define the chip area, which is required to calculate the cutting forces. The differential cutting edge length dS_j is multiplied with the edge force coefficients to calculate edge forces. $\delta(z)$ is the Boolean function showing whether the cutting edge is in cut at the point of interest, which mainly depends on the information contained in the CWEB map as described in Sect. 3.

Chip width, db, is defined as the length of the tangent line of the cutting envelope for a differential axial length:

$$db = \frac{dz}{\sin\kappa(z)} \tag{14}$$

Cutting edge length, dS, at elevation z with axial element length of dz is written as follows:

$$dS = \left\| \begin{matrix} P_y(z) - P_x(z - \mathrm{d}z) \\ P_y(z) - P_y(z - \mathrm{d}z) \\ P_z(z) - P_z(z - \mathrm{d}z) \end{matrix} \right\| \tag{15}$$

The tangential, radial, and axial forces are transformed into tool coordinates considering a transformation in terms of axial and radial immersion angles, κ and ϕ:

$$\begin{bmatrix} dF_x \\ dF_y \\ dF_z \end{bmatrix} = T \begin{bmatrix} dF_r \\ dF_t \\ dF_a \end{bmatrix} \quad where \tag{16}$$

$$T = \begin{bmatrix} -\sin\phi_j\sin\kappa & -\cos\kappa & -\sin\phi_j\cos\kappa \\ -\cos\phi_j\sin\kappa & \sin\kappa & -\cos\phi_j\cos\kappa \\ -\cos\kappa & 0 & -\sin\kappa \end{bmatrix}$$

The total milling forces in tool coordinates at a radial immersion angle of ϕ are the summation of the contributions from all teeth in cut:

$$F_k(\phi) = \sum_{j=1}^{N_t} \sum_{i=0}^{L/\mathrm{dz}} \left(dF_{k,j}(\phi(i.\mathrm{dz})) \right) \; k = x,y,z \tag{17}$$

Finally, the total milling forces are expressed in process coordinates as follows:

$$\begin{bmatrix} F_F \\ F_C \\ F_N \end{bmatrix} = T_{FCN} \begin{bmatrix} F_x \\ F_y \\ F_z \end{bmatrix} \tag{18}$$

where T_{FCN} is the transformation matrix relating the tool coordinates to the process coordinates.

Uncut chip thickness definition for general cutting tools in multi-axis milling the chip thickness $h_j(\phi_j,z)$ is expressed in terms of the normal vector to the cutting edge, $\hat{n}$, feed vector, $\hat{f}$, and feed per tooth, $f_{t,j}(z)$, for general milling tools:

$$h_j(\phi_j,z) = \left(\hat{n} \cdot \hat{f} \right) f_{t,j}(z) \tag{19}$$

As a convention, the feed vector is always considered in plane with tool x direction. Thus, the feed unit vector in tool coordinates can be represented as vector formed by the planar feed, $\hat{f}_{xy}$, and the axial feed, $\hat{f}_z$:

$$\hat{f} = \begin{bmatrix} \hat{f}_{xy} \\ 0 \\ \hat{f}_z \end{bmatrix} \tag{20}$$

The cutting edge point unit outward vector, $\hat{n}$, is defined as follows:

$$\hat{n} = \begin{bmatrix} \sin\kappa\sin\phi_j \\ \sin\kappa\cos\phi_j \\ -\cos\kappa \end{bmatrix} \tag{21}$$

The general chip thickness Eq. (19) can be written in planar and axial directions as follows:

$$h_j(\phi_j,z) = \left(\hat{f}_{xy}\sin\phi_j\sin\kappa - \hat{f}_z\cos\kappa \right) f_{t,j}(z) \tag{22}$$

For milling tools having N_t number of cutting edges with variable helix and variable pitch angle, the feed per tooth value is simply expressed as follows:

$$f_{t,j}(z) = \frac{feed}{n} \frac{\delta\phi(z)}{2\pi} \tag{23}$$

Variable helix and variable pitch angles introduce varying time delay between successive cutting edges represented by $\delta\phi_j(z)$ (Eq. (7)). The wavy form along the cutting edges, i.e., the serrations, introduces variations on the local radius along the tool axis, which is ground radially with a phase difference in the wave profile among consecutive cutting flutes. In Fig. 8, the phase difference between adjacent teeth is demonstrated. For equally separated milling cutters, the phase shift for the j^{th} flute is expressed as follows:

$$\theta_{s,j} = 2\pi\frac{j-1}{N_t} \tag{24}$$

In general, the chip load is nonuniformly distributed both among the cutting flutes and along the tool axis due to serrations as mentioned above. This is because the portion of the cutting edge engaged with the material removes the thicker chip as some parts of the cutting edge do not engage with the material as shown in Fig. 8.

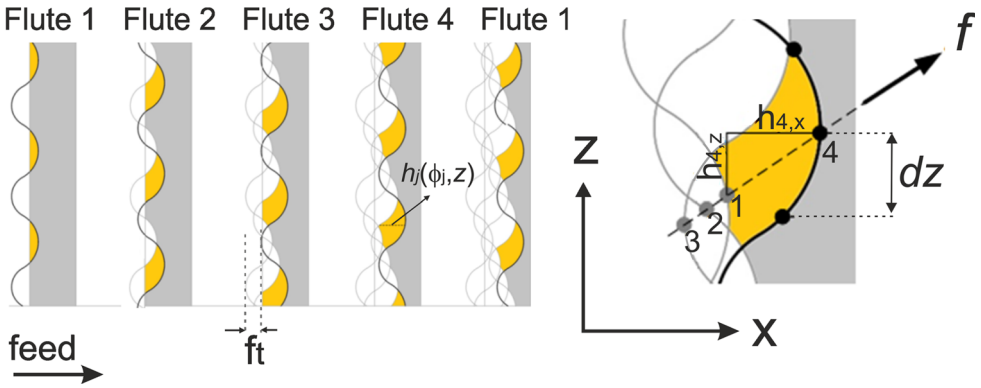

(a) chip distrubution over the cutting flutes (b) chip thickness in multi-axis milling

Fig. 8 Illustration of chip load of a sample serrated cutter. **a** Chip distribution over the cutting flutes. **b** Chip thickness in multi-axis milling

The chip thickness variation of a serrated cutter is similar to the case with run-out at a local axial level, which is given by Kline and Devor [20] and Wang and Liang [26] for 2D milling operations. Hence, the definition of the uncut chip thickness for a serrated end milling tool is written as follows:

$$h_{j,x}(\phi_j,z) = \min_{m=1\ldots N_t}\left[\left(\sum_{j=1}^{m} f_{t,j}(z)\right)\widehat{f}_x\sin(\phi_j) + \Delta r_{eff}\right]\sin\kappa_j(z) \tag{25}$$

where the effective radius difference, Δr_{eff} is defined as follows:

$$\Delta r_{eff} = r_j(z) - r_{j-m}\left(z - \widehat{f}_z\sum_{p=1}^{m} f_{t,p}(z)\right) \tag{26}$$

The effect of serration can be observed if the following condition is satisfied:

$$\left(\sum_{p=1}^{m} f_{t,j}(z)\right)\sin\phi_j < r_j(z) - r_{j-m}(z) \tag{27}$$

On the other hand, the uncut chip thickness in z direction is not affected by this mechanism and can simply be written as follows:

$$h_{j,z}(\phi_j,z) = \left(\widehat{f}_z.f_{t,j}(z)\right)\cos\kappa(z) \tag{28}$$

A comparison between the chip loads along the cutter axis of tools with uniform, variable helix-pitch, and serrated flutes is demonstrated in Fig. 9, where a half immersion down milling with feed per tooth of 0.1 mm is considered. The first tool has uniform flutes with 30° helix angle. In Fig. 9a, it is seen that the maximum chip load for each flute is 0.1 mm and equal to each other. The helix distribution of the second tool is 30°–36°–30°–36°, and the pitch angle alternates by ΔP which is 10°.

5 Experimental verification

The proposed general force model is verified by several standard and custom-made milling tools. The cutting tests were performed on DMG DMU 50evo five-axis

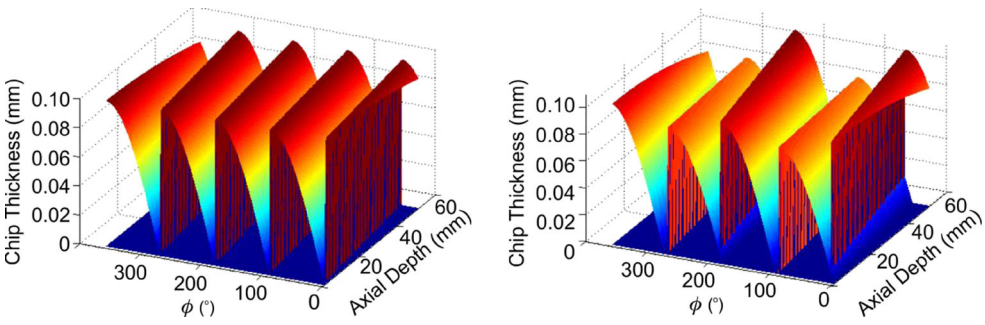

(a) Tool 1: Uniform flutes (b) Tool 2: Non-uniform flutes

Fig. 9 Comparison of tools having uniform and nonuniform flutes. **a** Tool 1, uniform flutes. **b** Tool 2, nonuniform flutes

Table 2 Experimental cases considered for verification

	Case 1	Case 2	Case 3	Case 4	Case 5	Case 6
Tool type	Bull nose end mill	Profile tool	Flat end mill	Flat end mill	Taper ball end mill	Ball end mill
Tool diameter (mm)	12	68.3	12	12	10	12
No. of flutes	2	18	3	4	5	2
Helix angle (deg)	0	0	30	Variable	30	30
Taper angle (deg)	0	0	0	0	2	0
Process parameters						
Material	AL7075	Ti6Al4V	AL7075	Al7075		
Cutting depth (mm)	3	20.2	4	7.5	23	1.5
Step over (mm)	7	2	9	5	Slotting	3.6, 2.4, 4.6
Cutting mode	Up	Down	Down	Down	Slotting	Down
Lead/tilt (deg)	30/−15	0/0	0/0	0/0	8/0	[6, 24][6, 12][18, 30]
Feed rate (um/rev)	250	50	15/75	50	16	100
Speed (rpm)	4,000	1,400	1,200	2,650	600	3,000
Material database						
	AL7075			Ti6Al4V		
τ_s (MPa)	297.05+1.05αr			613		
β_f (deg)	18.79+6.7h+0.0076Vc+0.256αr			19.1+0.29α		
ϕ_c (deg)	24.2+36.67h+0.0049V_c+0.3α_r			$r = r_0 h^a,\ r_0 = 1.755-0.028\alpha\ \ a = 0.331-0.0082\alpha$		
K_{te} (N/mm)	23			24		
K_{re} (N/mm)	35			43		

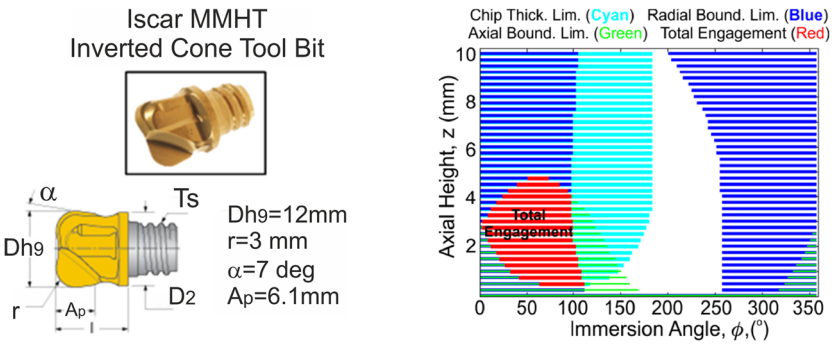

(a) Detailed drawing of the tool used in case 1. (b) 2D engagement boundaries.

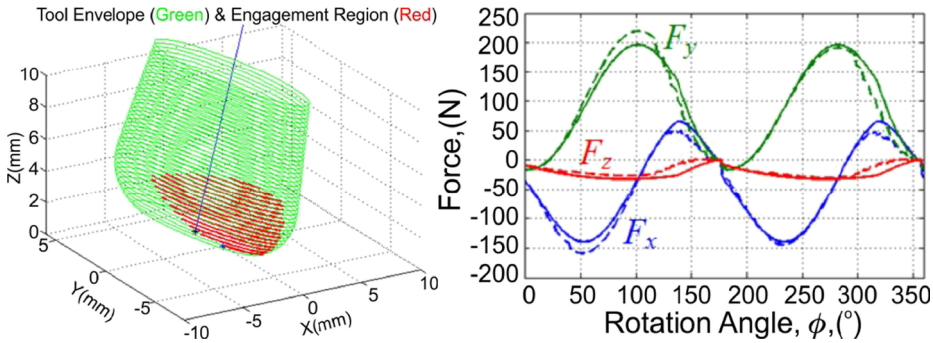

(c) 3D engagement boundaries. (d) Simulated (-) and measured (---) cutting forces

Fig. 10 Results of verification case 1. **a** Detailed drawing of the tool used in case 1. **b** 2D engagement boundaries. **c** 3D engagement boundaries. **d** Simulated (-) and measured (—) cutting forces

milling center, where the cutting forces were measured by Kistler table-type dynamometer (Type 9275BA) and Kistler rotating dynamometer (Type 9123C). The model predictions are verified through five cases given in Table 2, where the tool geometry, cutting conditions, and the orthogonal cutting database for the materials used in the experiments are given.

5.1 Case 1: bull nose end mill

In case 1, a standard inverted cone bull end mill shown in Fig. 10a is used in five-axis milling of AL7075-T6. In the simulations, 0.25 mm of disk height and 1° of angular step size are used. The engagement boundary is plotted in Fig. 10b, c where it is seen that the calculated engagement boundary is smooth and continuous. The comparison of the measured and simulated forces is given in Fig. 10d which shows good agreement. The slight deviations in the peak force amplitudes are due to the run-out of the cutting tool.

5.2 Case 2: profiling

The second test is performed to verify the validity of the proposed model for multi-segmented cutting tools, where a custom profiling tool shown in Fig. 11a is used. The tool

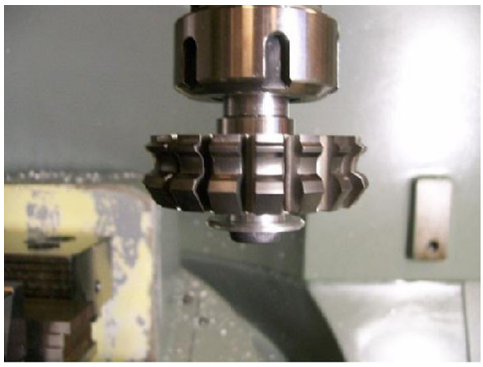

(a) Profiling tool used in the test.

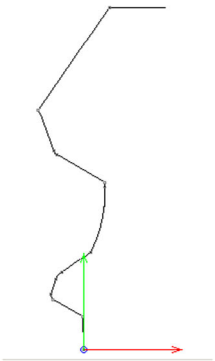

(b) Measured profile of the tool

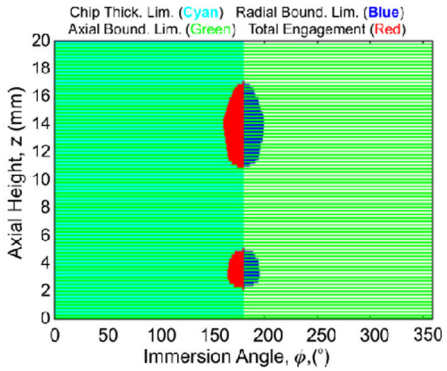

(c) 2D cutter engagement boundary

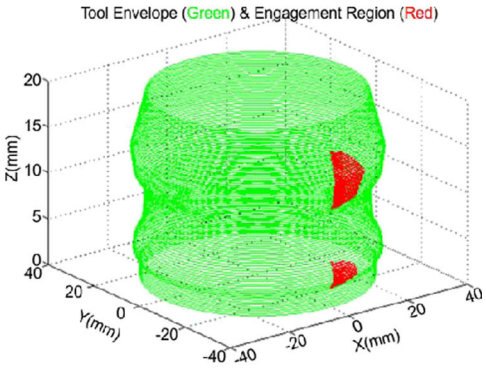

(d) 3D cutter engagement boundary

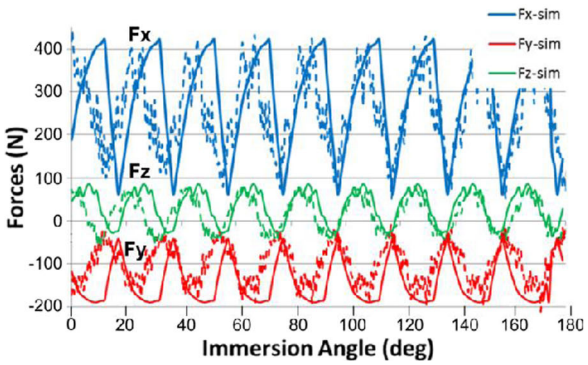

(e) Simulated (-) and measured (---) cutting forces

Fig. 11 Tool geometry, simulation, and experimental results for case 2. **a** Profiling tool used in the test. **b** Measured profile of the tool. **c** 2D cutter engagement boundary. **d** 3D cutter engagement boundary. **e** Simulated (-) and measured (—) cutting forces

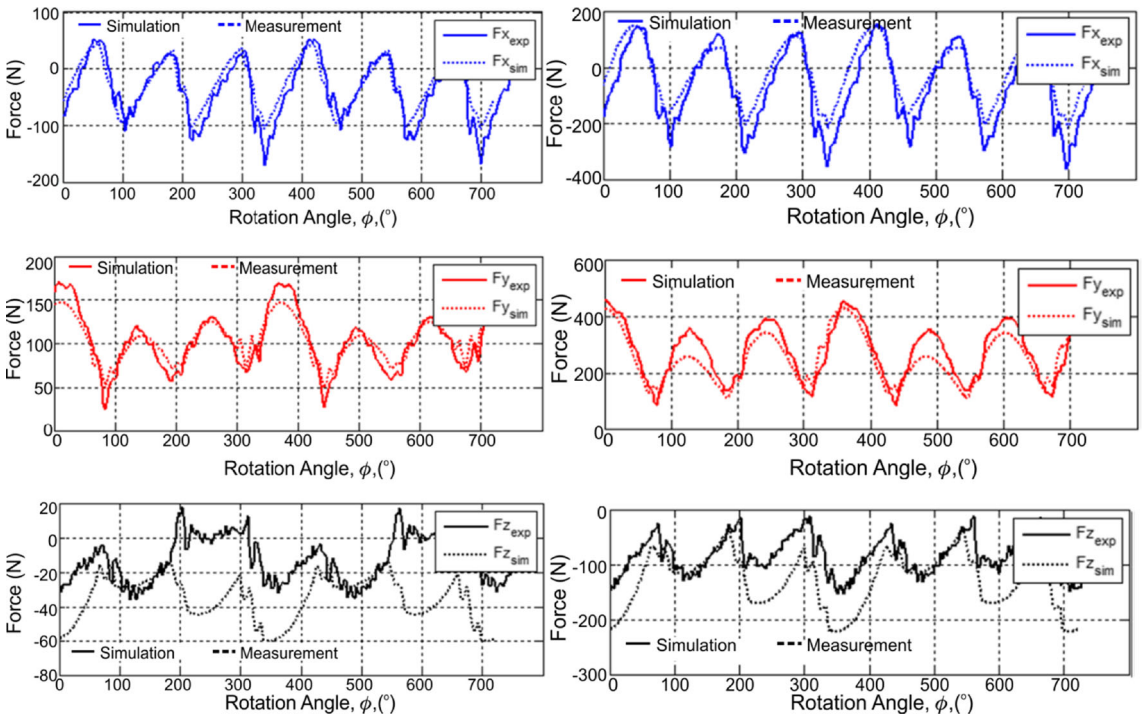

(a) 0.015 mm/rev feed rate. (b) 0.075 mm/rev feed rate.

Fig. 12 Results of case 3. **a** 0.015 mm/rev feed rate. **b** 0.075 mm/rev feed rate

profile measured using an optic CMM e is shown in Fig. 11b. The tool has 18 straight cutting edges. The tool profile is composed of eight linear and four circular segments with a diameter and flute length of 68.3 and 20.2 mm, respectively. These types of custom profiling tools are used to engrave the edge profile directly on the cur surface. Thus, the verification test is performed at two-and-a-half-axis conditions with 2-mm radial depth of cut. The 2D and 3D cutter engagement boundary is shown in Fig. 11c, d, respectively. The engagement boundaries are calculated, and the simulations are performed using 0.2 mm of disc height and 1° of angular step size.

The measurement and simulation results for the cutting forces are shown in Fig. 11e which shows reasonably good agreement. The measurement data is noisy, but there was no chatter during the cut. There exists a small delay in the tooth periods which can be due to the deviation in the spindle speed during cutting.

5.3 Case 3: serrated flat end mill

In case 3, the milling forces are measured in machining of AL7075–T6 with a serrated end mill having circular serration profile known as DIN 844 NF standard. The serration form has 2-mm wavelength and 0.3-mm amplitude. The effect of feed rate is demonstrated by using two feed rates. The simulated and measured forces are compared for feed rates of 0.015 and 0.075 mm/tooth in Fig. 12a, b, respectively.

5.4 Case 4: variable helix flat end mill

In case 4, the verification is performed for tools with nonuniform cutting flute geometries by machining of AL7075–T6. Two cutting tools, one having variable helix and one having both variable helix and pitch angles, are used in the tests, where the tool geometries are defined in Table 3. In order to capture the separation angle along the

Table 3 Cutting edge geometry used in case 5

Tool code	Helix angle (deg), $i_{0,1\ldots4}$	Pitch distribution type	Pitch angles (deg) $\phi_{p,1\ldots4}(0)$
AOT.318.002	30–32–34–36	–	90–90–90–90
AOT.318.003	30–33–30–33	Alternating	87–93–87–93

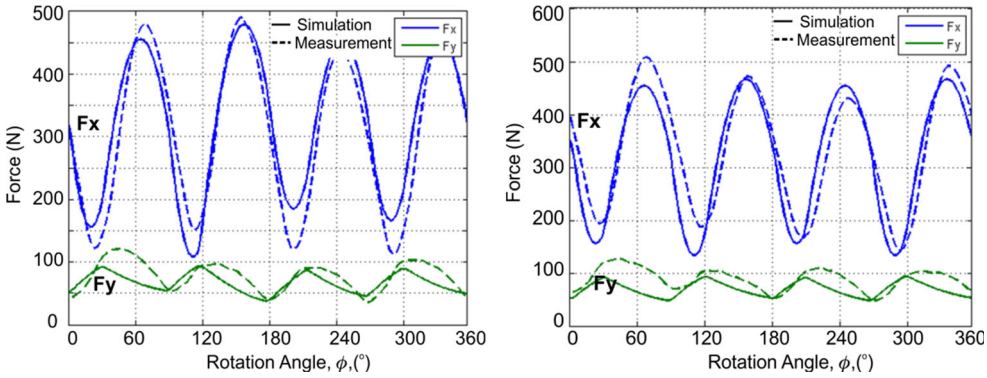

Fig. 13 Results of case 4

tool body, a relatively deep cutting condition is chosen. The measured cutting forces are compared with the simulations in Fig. 13, where a reasonable agreement is observed.

5.5 Case 5: flank milling

A representative five-axis milling process with a serrated taper ball end mill, i.e., hog mill, is studied in this case. This type of an operation is a typical roughing cycle for machining of integrally bladed rotors where the chip load is relatively high as the cutting depth is selected as high as the flute length. However, the cutting depth is not selected that is high for this demonstration. The workpiece material is Ti6Al4V. In the machining experiment, the cutting forces are measured using Kistler 9123C rotary dynamometer as shown in Fig. 14a. As $-x$ and $-y$ directions are in the rotary frames, it is possible to do the comparison in terms of the resultant cutting force perpendicular to the cutting tool, i.e., F_{xy}, and the axial cutting force F_z. To do so, the measured forces in rotating $-x$ and $-y$ directions are used to calculate F_{xy}. The measured and simulated F_{xy} and F_z are compared in Fig. 14b.

The simulations and measurements show reasonable agreement except some discrepancy that may be caused due to measurement errors and approximations in the cutting force model. However, it can be concluded that the cutting forces are estimated with an acceptable error margin for that complex five-axis cycle, where the cutting tool has a tapered envelope and serrated edges.

5.6 Case 6: ball end milling

Ball end milling is one of the most commonly used machining technologies in multi-axis milling for roughing, semi-finishing, and finishing purposes. Thus, the validity of any model developed for simulation of multi-axis milling with generalized cutting tool geometry needs to be verified. The proposed model is verified through ball end milling tests at three conditions with different step over values and tool orientation vectors as given in Table 2, where the cutting tool is 12-mm diameter ball end mill with two regular cutting edges.

The comparison between the simulated and measured cutting forces is given in Fig. 15. It is seen that the cutting forces are estimated in a reasonable accuracy. However, there is slight discrepancy in example 2. This may be due to the radial run-out of the cutting tool, where the peak values in the forces show 60 N difference.

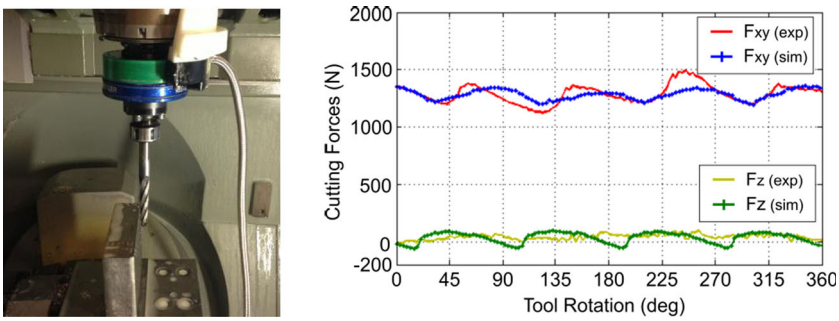

(a) Test setup (b) Simulated and measured cutting forces

Fig. 14 Results of case 5. **a** Test setup. **b** Simulated and measured cutting forces

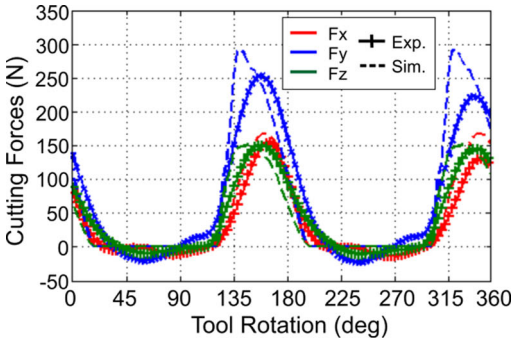

(a) Case 6-1: Lead 6 deg, Tilt=24 deg, Step over 30%

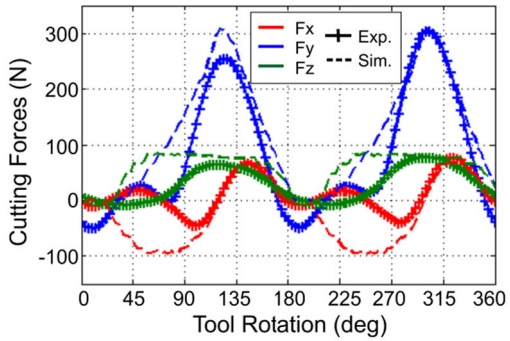

(b) Case 6-2: Lead 6 deg, Tilt=12 deg, Step over 20%

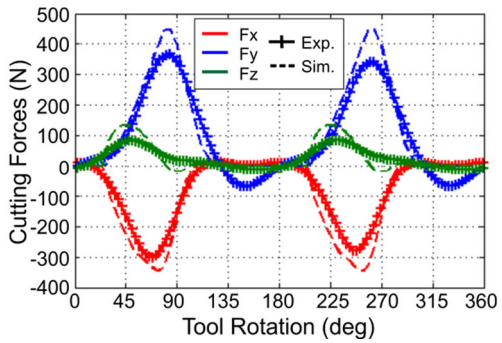

(c) Case 6-3: Lead 18 deg, Tilt= -30 deg, Step over 40%

Fig. 15 Results of case 6. **a** Case 6-1: lead 6°, tilt=24°, step over 30 %. **b** Case 6-2: lead 6°, tilt=12°, step over 20 %. **c** Case 6-3: lead 18°, tilt= −30°, step over 40 %

6 Conclusion

In this paper, a generalized cutting force model for multi-axis milling is presented. The developed model includes the generalized definition of the cutting tool and cutting edge, generalized definition of chip thickness, and a new generalized approach for determination of the cutter-workpiece engagement boundaries. The cutting tool envelope is defined as a revolved surface of a multi-segmented section, which is composed of arcs and lines. The generalized chip thickness definition is used to conform to the generalized cutting edge definition in order to cover tools with irregular cutting edge geometry such as serrated, variable pitch, and variable helix tools. The performance of the new engagement boundary calculation approach is tested under various cases, and it is shown that the method works in linear complexity contrary to common discretization methods. The accuracy of the simulations is verified through series of cutting tests in six cases. Each of these cases would represent different applications in machining industry under various conditions such as roughing, semi-finishing, or finishing using several cutting tools. In general, it is seen that the simulations agree well with the measurements except slight discrepancies at random conditions.

References

1. Martelotti ME (1941) An analysis of milling process. Trans ASME 122:3–11
2. Koenigsberger R, Sabberwal AJP (1961) An investigation into the cutting force pulsations during milling operations. Int J Mach Tool Des Res 1:15–33
3. Kline WA, DeVor RE, Lindberg JR (1982) The prediction of cutting forces in the end milling with application to cornering cuts. Int J Mach Tool Des Res 22:7–22
4. Altintas Y, Spence A (1991) End milling force algorithms for CAD systems. CIRP Ann 40:7–22
5. Budak E, Altintas Y, Armarego EJA (1996) Prediction of milling force coefficients from orthogonal cutting data. Trans ASME 118: 216–224
6. Armarego EJA, Epp CJ (1970) An investigation of zero helix peripheral up-milling. Int J Mach Tool Des Res 10:273–291
7. Lee P, Altintas Y (1996) Prediction of ball-end milling forces from orthogonal cutting data. Int J Mach Tools Manuf 36:1059–1072
8. Engin S, Altıntaş Y (2001) Mechanics and dynamics of general milling cutters. Part I: helical end mills. Int J Mach Tools Manuf 41:2213–2231
9. Engin S, Altıntaş Y (2001) Mechanics and dynamics of general milling cutters. Part II: inserted cutters. Int J Mach Tools Manuf 41: 2195–2212
10. Merdol DS, Altintas Y (2004) Mechanics and dynamics of serrated cylindrical and tapered end mills. J Manuf Sci E-T ASME 126:317–326
11. Kaymakci M, Kilic ZM, Altintas Y (2012) Unified cutting force model for turning boring, drilling and milling operations. Int J Mach Tools Manuf 55:34–45
12. Lazoglu I, Liang SY (1996) Modeling of ball-end milling forces with cutter inclination. J Manuf Sci Eng 122:3–11
13. Ozturk E, Budak E (2007) Modeling of 5-axis milling processes. Mach Sci Technol 11/3:pp. 287–pp. 311
14. Ferry WB, Altintas Y (2008) Virtual five-axis flank milling of jet engine impellers—part I-II. J Manuf Sci Eng 130:011005
15. Lopez de Lacalle LN, Lamikiz A, Munoa J, Salgado MA, Sanchez JA (2006) Improving the high-speed finishing of forming tools for advanced high-strength steels (AHSS). Int J Adv Manuf Technol 29: 49–63
16. Lia XP, Zhenga HQ, Wonga YS, Neea AYC (2000) An approach to theoretical modeling and simulation of face milling forces. J Manuf Process 2(4):225–240

17. Siller HR, Vila C, Rodriguez CA, Abellan JV (2008) Study of face milling of hardened AISI D3 steel with a special design of carbide tools. Int J Adv Manuf Technol 40:12–25
18. Campomanes ML (2002) Kinematics and dynamics of milling with roughing end mills. Metal Cutting and High Speed Machining, Kluwer Academic/Plenum Publishers
19. Kim S-J, Lee H-U, Cho DW (2006) Feedrate scheduling for indexable end milling process based on an improved cutting force model. Int J Mach Tools Manuf 46:1589–1597
20. Kline WA, DeVor RE (1983) The effect of runout on cutting geometry and forces in end milling. Int J Mach Tool Des Res 23(2–3):123–140
21. Ramaraj TC, Eleftheriou E (1994) Analysis of mechanics of machining with tapered end milling cutters. Trans ASME 116:398–404
22. Budak E (2003) An analytical design method for milling cutters with nonconstant pitch to increase stability part 2: application. J Manuf Sci Eng 125:35–38
23. Hormann K, Agathos A (2001) The point in polygon problem for arbitrary polygons. Comput Geom 20(3):131–144
24. Özlü E, Budak E, Molinari A (2007) Thermomechanical modeling of orthogonal cutting including the effect of stick-slide regions on the rake face. 10th International Workshop on Modeling of Machining Operations
25. Budak E, Ozlu E (2008) Development of a thermo-mechanical cutting process model for machining process simulations. CIRP Ann Manuf Technol 57(1):97–100
26. Junz WJ-J, Liang SY (1996) Chip load kinematics in milling with radial cutter runout. Trans ASME 118:111–118